LETTER

Deterministic quantum state transfer and remote entanglement using microwave photons

P. Kurpiers[1,4]*, P. Magnard[1,4], T. Walter[1], B. Royer[2], M. Pechal[1], J. Heinsoo[1], Y. Salathé[1], A. Akin[1], S. Storz[1], J.-C. Besse[1], S. Gasparinetti[1], A. Blais[2,3] & A. Wallraff[1]*

Sharing information coherently between nodes of a quantum network is fundamental to distributed quantum information processing. In this scheme, the computation is divided into subroutines and performed on several smaller quantum registers that are connected by classical and quantum channels[1]. A direct quantum channel, which connects nodes deterministically rather than probabilistically, achieves larger entanglement rates between nodes and is advantageous for distributed fault-tolerant quantum computation[2]. Here we implement deterministic state-transfer and entanglement protocols between two superconducting qubits fabricated on separate chips. Superconducting circuits[3] constitute a universal quantum node[4] that is capable of sending, receiving, storing and processing quantum information[5–8]. Our implementation is based on an all-microwave cavity-assisted Raman process[9], which entangles or transfers the qubit state of a transmon-type artificial atom[10] with a time-symmetric itinerant single photon. We transfer qubit states by absorbing these itinerant photons at the receiving node, with a probability of 98.1 ± 0.1 per cent, achieving a transfer-process fidelity of 80.02 ± 0.07 per cent for a protocol duration of only 180 nanoseconds. We also prepare remote entanglement on demand with a fidelity as high as 78.9 ± 0.1 per cent at a rate of 50 kilohertz. Our results are in excellent agreement with numerical simulations based on a master-equation description of the system. This deterministic protocol has the potential to be used for quantum computing distributed across different nodes of a cryogenic network.

Remote entanglement has been realized probabilistically using heralded or unheralded protocols based on measurement projection[11–14], single-[15,16] or two-photon[17–20] detection or direct transfer of a single photon[21,22]. See Methods and Extended Data Fig. 1 for an overview of selected experimental results, including a discussion of concurrent deterministic experiments performed with superconducting circuits[23,24]. However, a fully deterministic implementation[25] of direct transfer protocols is more challenging to realize. In the protocol[25], a stationary atom is coupled to a single-mode cavity in remote quantum nodes and a coherent drive entangles the state of the atom with the field of the cavity. The cavity is coupled to a directional quantum channel into which the field is emitted as a time-symmetric single photon. This photon travels to the receiving node where it is ideally absorbed with unit probability using the time-reversed coherent drive (Fig. 1a). In addition to establishing entanglement between the nodes, direct transfer of quantum information offers the possibility to transmit arbitrary qubit states from one node to the other.

In our adaptation of this scheme (Fig. 1b) to the circuit quantum electrodynamic architecture, each quantum node (labelled A and B) is composed of a superconducting transmon qubit with transition frequency $\nu_{\mathrm{ge}}^{\mathrm{A}} = 6.343$ GHz or $\nu_{\mathrm{ge}}^{\mathrm{B}} = 6.093$ GHz dispersively coupled to two coplanar microwave resonators, analogous to an atom coupled to two cavity modes. One resonator is dedicated to dispersive transmon read-out and the other to excitation transfer. The transfer resonators at the

two nodes are tuned to have matching frequencies $\nu_{\mathrm{T}} \approx 8.400$ GHz and large bandwidths $\kappa_{\mathrm{T}}/(2\pi)$ of the order of 10 MHz (see Methods). All resonators are coupled to dedicated filters, to protect the transmons from Purcell decay[26,27]. An external coaxial line with a length of 0.9 m, bisected with a circulator, connects the transfer circuits of both chips. With this set-up, photons are routed from node A to B and from node B to a detection line. If perfect absorption of the photon can be realized and independent detection of the photon is not needed or desired, then the circulator can be omitted from the circuit[25]. To generate a controllable light–matter interaction, we apply a coherent microwave tone to the transmon, which induces an effective interaction $\tilde{g}(t)$ with tunable amplitude and phase[9,28] between states $|f, 0\rangle$ and $|g, 1\rangle$. Here, $|s, n\rangle$ denotes a Jaynes–Cummings dressed eigenstate with transmon state $|s\rangle$ and Fock state of the transfer resonator $|n\rangle$. The two lowest-energy eigenstates ($|g\rangle$ and $|e\rangle$) of the transmon form the qubit subspace; the second excited state ($|f\rangle$) is used as an auxiliary level to control the light–matter interaction in our experiment. This interaction swaps an excitation from the transmon to the transfer resonator, which then couples to a mode propagating towards node B. By controlling $\tilde{g}(t)$ (see Methods), we shape the itinerant photon to have a time-symmetric envelope $\phi(t) = \frac{1}{2}\sqrt{\kappa_{\mathrm{eff}}} \operatorname{sech}(\kappa_{\mathrm{eff}} t/2)$, with an adjustable photon bandwidth κ_{eff} limited only by κ_{T}. By inducing the reverse process $|g, 1\rangle \leftrightarrow |f, 0\rangle$ with the time-reversed amplitude and phase profile of $\tilde{g}(t)$, we absorb the itinerant photon in the transmon at node B. Ideally, this procedure returns all photonic modes to their vacuum state. We note that in our system this process could also be implemented with asymmetric photon shapes, or ones with a more structured time dependence[29], as long as the physical constraints on the bandwidth required for its emission and absorption are met at the respective sites.

To characterize the excitation transfer, we start by initializing the transmon in its ground state[30], after which we apply a sequence of two π pulses (R_{ge}^{π}, R_{ef}^{π}) to prepare the transmon at the receiving node B in state $|f, 0\rangle$. Next, we induce the effective coupling $\tilde{g}(t)$ with a modulated drive R_{f0g1}^{τ} to emit a symmetric photon[9] (Fig. 2a). We vary the instantaneous frequency of R_{f0g1}^{τ} to compensate for the drive-amplitude-dependent a.c. Stark shift of the $|f, 0\rangle \leftrightarrow |g, 1\rangle$ transition (see Methods). Here, and in all subsequent measurements, the population of the transmon states are extracted using single-shot readout with a correction to account for measurement errors (see Methods). The populations of the three lowest levels of the transmon $P_{\mathrm{g,e,f}}$ are measured immediately after truncating the emission pulse R_{f0g1}^{τ} at time τ (Fig. 2b). In this way, we observe that the transmon evolves smoothly from $|f\rangle$ to $|g\rangle$ during the emission process. At the end of the protocol, the emitting transmon reaches a ground-state population of $P_{\mathrm{g}} = 95.8\%$, which characterizes the emission efficiency.

To verify that the envelope of the emitted photon has the target shape and bandwidth $\kappa_{\mathrm{eff}}^{\mathrm{B}}/(2\pi) = 10.6$ MHz, we repeat the emission protocol with an initial transmon state $(|g\rangle + |f\rangle)/\sqrt{2}$ and measure the averaged electric-field amplitude $\langle a_{\mathrm{out}}(t)\rangle \propto \phi(t)$ of the emitted photon

[1]Department of Physics, ETH Zürich, Zürich, Switzerland. [2]Institut Quantique and Département de Physique, Université de Sherbrooke, Sherbrooke, Québec, Canada. [3]Canadian Institute for Advanced Research, Toronto, Ontario, Canada. [4]These authors contributed equally: P. Kurpiers, P. Magnard. *e-mail: philipp.kurpiers@phys.ethz.ch; andreas.wallraff@phys.ethz.ch
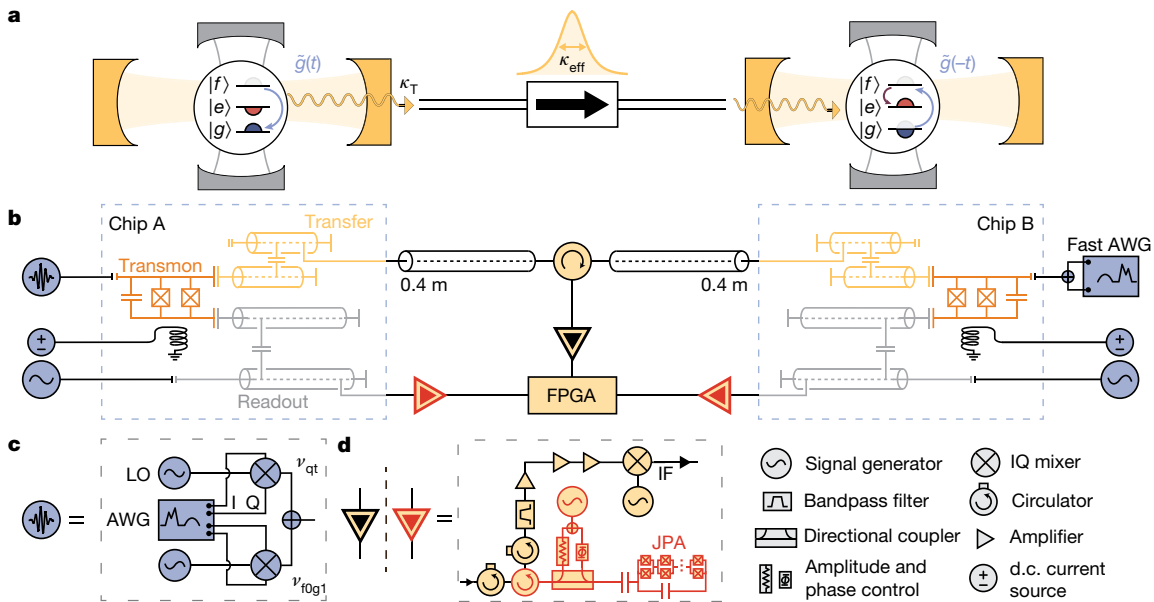
Fig. 1 | Schematic and measurement set-up. a, Quantum optical schematic of a deterministic unidirectional entanglement protocol between two cavity quantum electrodynamic nodes of a quantum network. At the first node, a three-level system is prepared in its second excited state $|f\rangle$ (grey half-circle) and driven coherently ($\tilde{g}(t)$, blue arrow) to $|g\rangle$ (blue half-circle), creating the transfer cavity field $|1\rangle$ (light yellow). The cavity field couples into the directional quantum channel with rate κ_T as a single-photon wavepacket with an effective bandwidth κ_{eff} (yellow hyperbolic secant shape). In the second quantum node, the time-reversed drive $\tilde{g}(-t)$ transfers the excitation from $|g\rangle$ to $|f\rangle$ in the presence of the transferred photon field $|1\rangle$. Finally, the protocol is completed with a transfer pulse between $|f\rangle$ and $|e\rangle$ (red half-circle) to return to the qubit subspace. In addition, each three-level system is coupled to a readout cavity (grey). **b**, Implementation of the system depicted in **a** in a planar, chip-based, circuit quantum electrodynamic architecture (Extended Data Fig. 2). At each node, a transmon (orange) is coupled capacitively to two $\lambda/4$ coplanar waveguide resonators and Purcell filter circuits[27] that act as the transfer (yellow) and readout (grey) cavities, respectively. The output transmission lines are coupled galvanically to the corresponding circuit. A directional

quantum channel is realized using a semi-rigid coaxial cable and a circulator connecting to the output port of the transfer circuit Purcell filter at each node. **c, d**, Details of the circuit quantum electrodynamic implementation. **c**, Combined qutrit (ν_{qt}) and $|f, 0\rangle \leftrightarrow |g, 1\rangle$ transition (ν_{f0g1}) microwave drive using single-side-band modulation with in-phase (I) and quadrature (Q) mixers driven by a local oscillator (LO) and with an envelope defined by an arbitrary-waveform generator (AWG) for node A. At node B, these drives are synthesized directly by a fast AWG with 25 GS s^{-1}. **d**, Schematic of microwave detection lines (black, red triangles). All detection lines consist of two isolators, a bandpass filter, a cryogenic amplifier (HEMT) and two room-temperature amplifiers followed by a filter and analogue down-conversion to an intermediate frequency of 250 MHz. The down-converted signal is lowpass-filtered, digitized using an analogue-to-digital converter and recorded using a field-programmable gate array (FPGA). The transmon-readout lines include an additional Josephson parametric amplifier (JPA) circuit (red elements) between the first two isolators. The JPA is pumped by a signal generator and the reflected pump signal from the JPA is cancelled at a directional coupler using amplitude- and phase-controlled destructive interference.

state $(|0\rangle + |1\rangle)/\sqrt{2}$ using heterodyne detection[31] (Fig. 2c). We prepare this photon state because of its non-zero average electric field[9].

Repeating the emission protocol from node A leads to similar dynamics of the transmon population (Fig. 2e). We adjust the amplitude and phase of the transfer pulse (Fig. 2d) so that the photons emitted from each node A and B have similar effective bandwidth κ_{eff} in spite of their respective transfer resonator bandwidths κ_T differing by approximately 30% (see Methods). The detected integrated power $\int |\langle a_{out}(t)\rangle|^2 \, dt$ of the photon emitted from node A (Fig. 2f) is $l_{AB} = 23.0\% \pm 0.5\%$ lower than that emitted from node B owing to loss accumulated as the photon travels from node A to B. The photon loss l_{AB} is extracted from the ratio of the integrated photon powers for emission from nodes B and A (see Methods). In addition, the envelope of the photon emitted from node A is slightly distorted by the reflection off node B, as determined by the response function of its transfer resonator, which is fully captured by our theoretical model.

To characterize the absorption of the single time-symmetric photon emitted from node A at the receiving node by time-reversing the emission pulse of node B (Fig. 2a, g), we measure the population of transmon B during the process. We apply a π pulse to transmon B to map $|f\rangle$ back to the qubit subspace before performing the readout. We observe the population of $|e\rangle$ to rise smoothly and saturate at $P_e^{sat} = 67.5\%$ (Fig. 2h). This saturation level reflects the efficiency of the protocol for the transfer of a single excitation (a single photon), which is executed in a pulse sequence of only 180-ns duration (Fig. 2g). From the ratio of the integrated power of the emitted photon in the absence

(Fig. 2i) or presence (Fig. 2f) of the absorption pulse, the absorption efficiency is determined to reach $98.1\% \pm 0.1\%$.

The results of master-equation simulations of the excitation transfer (solid lines in Fig. 2), using parameters extracted from independent measurements (see Methods), display excellent agreement with the measured data. This demonstrates a high level of control over the emission and absorption processes and an accurate understanding of the experimental imperfections dominated by qutrit decoherence and photon loss.

We demonstrate the use of our protocol to transfer deterministically an arbitrary qubit state from node A over a distance of about 0.9 m along a coaxial line to node B. This is realized by preparing the receiving transmon (B) in state $|g\rangle$, applying a R_{ef}^π pulse to the sending transmon (A), followed by the emission or absorption pulse and finally a rotation R_{ef}^π on transmon B. We characterize the quantum state transfer by reconstructing its process matrix χ with quantum process tomography (Fig. 3b). For that purpose, we prepare all six mutually unbiased qubit basis states[32] at node A, transfer them to node B, and reconstruct the transferred state using quantum state tomography (see Methods). We determine a process fidelity of $\mathcal{F}_p = tr(\chi\chi_{ideal}) = 80.02\% \pm 0.07\%$, well above the limit of 1/2 that can be achieved using local gates and classical communication only. The process matrix χ_{sim} calculated with the master-equation simulations agrees very well with the data (absolute values shown as red outlines in Fig. 3b). This is supported by the small trace distance[33] $tr|\chi - \chi_{sim}|/2 = 0.015$, which ideally is 0 for identical process matrices and 1 for orthogonal ones.
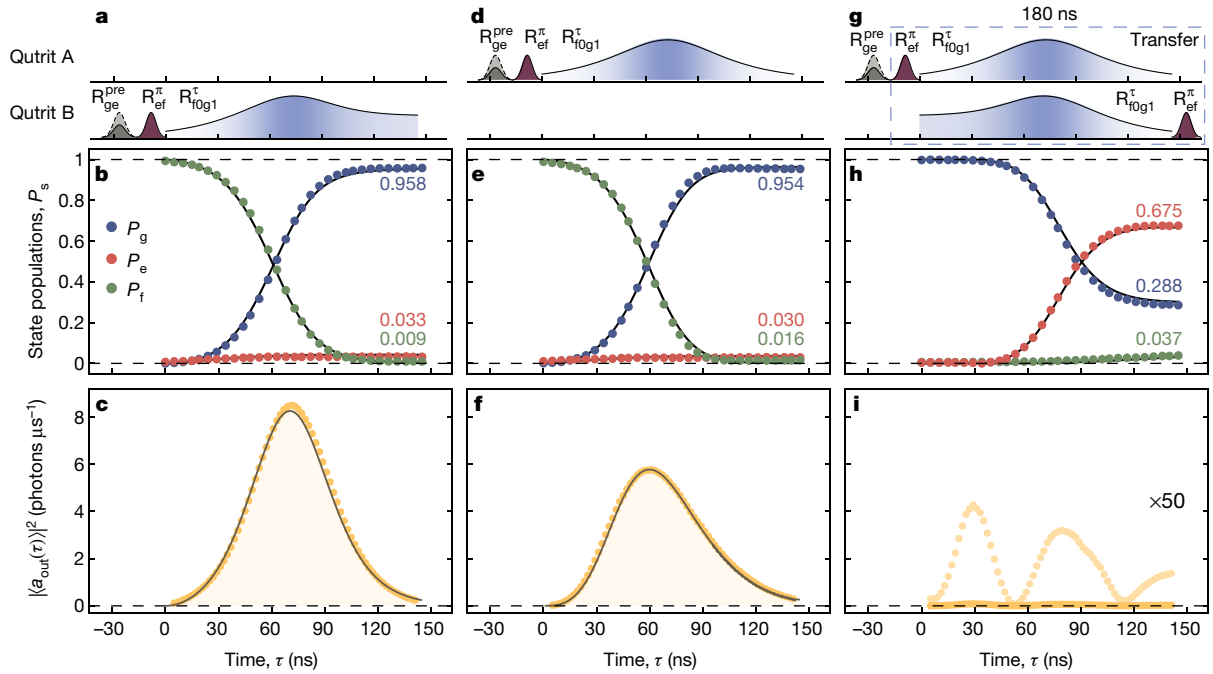
Fig. 2 | Emission, transfer and absorption of a single photon. a, d, The transmons at node B (**a**) and node A (**d**) are prepared in the state $|f\rangle$ using Gaussian derivative removal by adiabatic gate (DRAG) microwave pulses $R_{ge}^{pre=\pi}$ and R_{ef}^{π}. **b, e,** We characterize (filled circles) the time dependence (τ) of the qutrit populations $P_{g,e,f}$ while driving the $|f,0\rangle \leftrightarrow |g,1\rangle$ transition. The phase (white–blue shading) of the $|f,0\rangle \leftrightarrow |g,1\rangle$ transition drive is modulated to compensate the drive-induced quadratic a.c. Stark shift. **c, f,** The mean field amplitude squared $|\langle a_{out}(\tau)\rangle|^2$ of the travelling photons emitted from node B (**c**) and node A (**f**) is obtained for the photon state $(|0\rangle + |1\rangle)/\sqrt{2}$ that is emitted by preparing each transmon in $(|g\rangle + |f\rangle)/\sqrt{2}$ ($R_{ge}^{pre=\pi/2}$ in **a** and **d**). The effective photon bandwidths are adjusted to be $\kappa_{eff}^A/(2\pi) = 10.4$ MHz and $\kappa_{eff}^B/(2\pi) = 10.6$ MHz. The solid lines in **b, c, e, f, h** and **i** are results of master-equation simulations (see text for details). **g,** Excitation transfer protocol. **h,** The time dependence of $P_{g,e,f}$ when executing the excitation transfer protocol from qubit A to qubit B with $R_{ge}^{pre=\pi}$. **i,** The residual $|\langle a_{out}(\tau)\rangle|^2$ (light yellow, multiplied by 50) during the absorption process ($R_{ge}^{pre=\pi/2}$ in **g**).
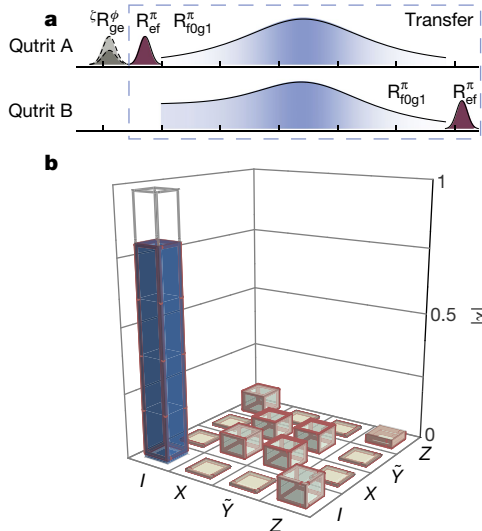
Fig. 3 | Quantum state transfer. a, Pulse scheme used to characterize the qubit state transfer between the two nodes. We prepare six mutually unbiased input states with rotations $^xR_{ge}^0$, $^xR_{ge}^{\pi/2}$, $^xR_{ge}^{-\pi/2}$, $^yR_{ge}^{\pi/2}$, $^yR_{ge}^{-\pi/2}$ and $^xR_{ge}^{\pi}$ at node A (denoted by $^\zeta R_{ge}^\phi$ where ζ is the rotation axis). **b,** We experimentally obtain a process matrix (absolute value $|\chi|$ shown as coloured bars in the basis of the Pauli matrices I, $X = \sigma_x$, $\tilde{Y} = i\sigma_y$ and $Z = \sigma_z$) with a fidelity of $\mathcal{F}_p = 80.02\% \pm 0.07\%$ relative to the ideal identity operation. The grey and red outlines show the ideal value and the master-equation simulation of the absolute values of the process matrix, respectively. The trace distance between the measurement and the simulation is 0.015.

Furthermore, we use the excitation transfer to generate two-qubit remote-entangled states between nodes A and B deterministically. The protocol starts by preparing transmons A and B in states $(|e\rangle + |f\rangle)/\sqrt{2}$ and $|g\rangle$, respectively, and then applying the emission or absorption pulses followed by a rotation R_{ef}^π on transmon B to generate the entangled Bell state $|\psi^+\rangle = (|e,g\rangle + |g,e\rangle)/\sqrt{2}$. Because leakage to the $|f\rangle$ level at both nodes leads to errors in the two-qubit density matrix reconstruction, we extract the full two-qutrit density matrix $\rho_{3\otimes3}$ from quantum state tomography experiments (see Methods). For illustration purposes, we display the two-qubit density matrix ρ_m (Fig. 4b, c), which consists of the two-qubit elements of $\rho_{3\otimes3}$. We find a state fidelity of $\mathcal{F}_{|\psi^+\rangle}^s = \langle\psi^+|\rho_m|\psi^+\rangle = 78.9\% \pm 0.1\%$ compared to the ideal Bell state, and a concurrence $\mathcal{C}(\rho_m) = 0.747 \pm 0.004$ (see Methods for a detailed discussion). The density matrix ρ_{sim} calculated from the master-equation simulations of the entanglement protocol (red outlines in Fig. 4) is in excellent agreement with the experimental results, displaying a small trace distance of $\mathrm{tr}|\rho_m - \rho_{sim}|/2 = 0.024$. We decompose the infidelity into approximately 10.5% from photon loss, 9% from finite transmon coherence times and 2% from pulse truncation.

Using transmons with relaxation and coherence times of $T_{1ge} = T_{2ge} = 30$ μs and $T_{1ef} = T_{2ef} = 20$ μs, and with an achievable 12% loss between the nodes, we calculate that our protocol would enable deterministic generation of remote-entangled states with a fidelity of 93%. In addition, we expect our protocol to be extendable to quantum network applications to generate deterministic heralded remote entanglement[4], using the three-level structure of the transmons and encoding quantum information in different time bins to detect photon loss. These perspectives indicate that the approach demonstrated here may serve as
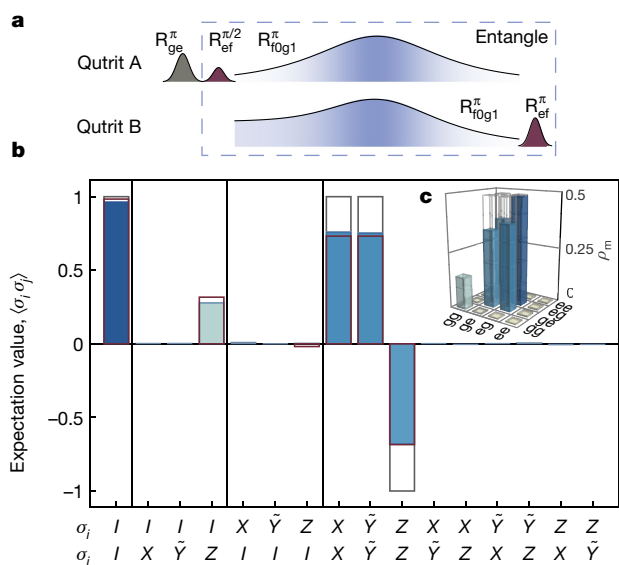
Fig. 4 | Remote-entanglement generation. a, Pulse scheme to generate deterministic remote entanglement between nodes A and B. **b**, Expectation values of two-qubit Pauli operators $\langle\sigma_i\sigma_j\rangle$. The coloured bars indicate the measurement results; the ideal expectation values for the Bell state $|\psi^+\rangle = (|e,g\rangle + |g,e\rangle)/\sqrt{2}$ and the results of a master-equation simulation are shown as grey and red outlines, respectively. We calculate a fidelity of $\mathcal{F}^s_{|\psi^+\rangle} = 78.9\% \pm 0.1\%$, which is well explained by photon loss and decoherence. **c**, Reconstructed density matrix ρ_m after execution of the remote-entanglement protocol.

the basis for distributed quantum computation in the circuit quantum electrodynamic architecture using distinct cryogenic nodes.

Online content

Any Methods, including any statements of data availability and Nature Research reporting summaries, along with any additional references and Source Data files, are available in the online version of the paper at https://doi.org/10.1038/s41586-018-0195-y.

1. Cirac, J. I., Ekert, A. K., Huelga, S. F. & Macchiavello, C. Distributed quantum computation over noisy channels. *Phys. Rev. A* **59**, 4249–4254 (1999).
2. Jiang, L., Taylor, J. M., Sørensen, A. S. & Lukin, M. D. Distributed quantum computation based on small quantum registers. *Phys. Rev. A* **76**, 062323 (2007).
3. Wallraff, A. et al. Strong coupling of a single photon to a superconducting qubit using circuit quantum electrodynamics. *Nature* **431**, 162–167 (2004).
4. Reiserer, A. & Rempe, G. Cavity-based quantum networks with single atoms and optical photons. *Rev. Mod. Phys.* **87**, 1379–1418 (2015).
5. Eichler, C. et al. Observation of entanglement between itinerant microwave photons and a superconducting qubit. *Phys. Rev. Lett.* **109**, 240501–240505 (2012).
6. Wenner, J. et al. Catching time-reversed microwave coherent state photons with 99.4% absorption efficiency. *Phys. Rev. Lett.* **112**, 210501 (2014).
7. Johnson, B. R et al. Quantum non-demolition detection of single microwave photons in a circuit. *Nat. Phys.* **6**, 663–667 (2010).
8. DiCarlo, L. et al. Demonstration of two-qubit algorithms with a superconducting quantum processor. *Nature* **460**, 240–244 (2009).
9. Pechal, M. et al. Microwave-controlled generation of shaped single photons in circuit quantum electrodynamics. *Phys. Rev. X* **4**, 041010 (2014).
10. Koch, J. et al. Charge-insensitive qubit design derived from the Cooper pair box. *Phys. Rev. A* **76**, 042319 (2007).
11. Julsgaard, B., Kozhekin, A. & Polzik, E. S. Experimental long-lived entanglement of two macroscopic objects. *Nature* **413**, 400–403 (2001).
12. Chou, C. W. et al. Measurement-induced entanglement for excitation stored in remote atomic ensembles. *Nature* **438**, 828–832 (2005).
13. Choi, K. S., Goban, A., Papp, S. B., van Enk, S. J. & Kimble, H. J. Entanglement of spin waves among four quantum memories. *Nature* **468**, 412–416 (2010).
14. Roch, N. et al. Observation of measurement-induced entanglement and quantum trajectories of remote superconducting qubits. *Phys. Rev. Lett.* **112**, 170501 (2014).
15. Slodička, L. et al. Atom-atom entanglement by single-photon detection. *Phys. Rev. Lett.* **110**, 083603 (2013).
16. Delteil, A. et al. Generation of heralded entanglement between distant hole spins. *Nat. Phys.* **12**, 218–223 (2016).
17. Moehring, D. L. et al. Entanglement of single-atom quantum bits at a distance. *Nature* **449**, 68–71 (2007).
18. Lee, K. C. et al. Entangling macroscopic diamonds at room temperature. *Science* **334**, 1253–1256 (2011).
19. Hofmann, J. et al. Heralded entanglement between widely separated atoms. *Science* **337**, 72–75 (2012).
20. Bernien, H. et al. Heralded entanglement between solid-state qubits separated by three metres. *Nature* **497**, 86–90 (2013).
21. Matsukevich, D. N. et al. Entanglement of remote atomic qubits. *Phys. Rev. Lett.* **96**, 030405 (2006).
22. Ritter, S. et al. An elementary quantum network of single atoms in optical cavities. *Nature* **484**, 195–200 (2012).
23. Axline, C. et al. On-demand quantum state transfer and entanglement between remote microwave memories. *Nat. Phys.* https://doi.org/10.1038/s41567-018-0115-y (2018).
24. Campagne-Ibarcq, P. et al. Deterministic Remote Entanglement of Superconducting Circuits through Microwave Two-Photon Transitions. *Phys. Rev. Lett.* **120**, 200501 (2018).
25. Cirac, J. I., Zoller, P., Kimble, H. J. & Mabuchi, H. Quantum state transfer and entanglement distribution among distant nodes in a quantum network. *Phys. Rev. Lett.* **78**, 3221–3224 (1997).
26. Reed, M. D. et al. Fast reset and suppressing spontaneous emission of a superconducting qubit. *Appl. Phys. Lett.* **96**, 203110 (2010).
27. Walter, T. et al. Rapid, high-fidelity, single-shot dispersive readout of superconducting qubits. *Phys. Rev. Appl.* **7**, 054020 (2017).
28. Zeytinoğlu, S. et al. Microwave-induced amplitude- and phase-tunable qubit-resonator coupling in circuit quantum electrodynamics. *Phys. Rev. A* **91**, 043846 (2015).
29. Kuhn, A., Hennrich, M. & Rempe, G. Deterministic single-photon source for distributed quantum networking. *Phys. Rev. Lett.* **89**, 067901 (2002).
30. Magnard, P. et al. Fast and unconditional all-microwave reset of a superconducting qubit. Preprint at https://arxiv.org/abs/1801.07689 (2018).
31. Bozyigit, D. et al. Antibunching of microwave-frequency photons observed in correlation measurements using linear detectors. *Nat. Phys.* **7**, 154–158 (2011).
32. van Enk, S. J., Lütkenhaus, N. & Kimble, H. J. Experimental procedures for entanglement verification. *Phys. Rev. A* **75**, 052318 (2007).
33. Nielsen, M. A. & Chuang, I. L. *Quantum Computation and Quantum Information* 10th edn, Ch. 9 (Cambridge Univ. Press, New York, 2011).

Author contributions The experiment was designed and developed by P.K., T.W., P.M. and M.P. The samples were fabricated by J.-C.B., T.W. and S.G. The experiments were performed by P.K., P.M. and T.W. The data were analysed and interpreted by P.K., P.M., B.R., A.B. and A.W. The FPGA firmware and experiment automation was implemented by J.H., Y.S., A.A., S.S., P.M. and P.K. The master-equation simulations were performed by B.R., M.P., P.M. and P.K. The manuscript was written by P.K., P.M., T.W., B.R. and A.W. All authors commented on the manuscript. The project was led by A.W.

Competing interests The authors declare no competing interests.

Additional information
Extended data is available for this paper at https://doi.org/10.1038/s41586-018-0195-y.
Reprints and permissions information is available at http://www.nature.com/reprints.
Correspondence and requests for materials should be addressed to P.K. or A.W.
Publisher's note: Springer Nature remains neutral with regard to jurisdictional claims in published maps and institutional affiliations.

METHODS

Literature overview. In Extended Data Fig. 1, we present a short overview of remote-entanglement experiments performed using the systems and schemes listed in the caption. We calculate bounds[34] on the concurrence $\mathcal{C}$ for papers in which a CHSH–Bell correlation S was specified but no value for $\mathcal{C}$ was given, to provide a more complete comparison. However, we do not calculate $\mathcal{C}$ for papers that provide only a Bell-state fidelity because knowledge of the elements of the density matrix are necessary to determine $\mathcal{C}$ without further assumptions.

In addition to the work described here, two independently performed experiments[23,24] concurrently realized deterministic remote state transfer and remote-entanglement generation with superconducting circuits along the lines of a previous proposal[25]. In contrast to our work, the other experiments[23,24] use three-dimensional cavities and transmon qubits with superior coherence properties instead of planar two-dimensional systems. They also use radiation fields with a Gaussian profile and a duration of 2–4 μs for state transfer and remote-entanglement generation—substantially longer than used here—which made use of dedicated Purcell filters to increase the emission and absorption bandwidth of the fields used for state transfer. As a result, the concurrence and fidelity found in our experiments exceed those found in the experiments in refs [23,24] at comparable absorption efficiencies and despite the inferior coherence times. Going beyond our work and that presented in ref. [24], ref. [23] presents transfer of multi-photon states and discusses the potential of the scheme for implementing error correction at each site.

We also note a measurement-based probabilistic realization of remote entanglement in superconducting circuits[35] that improves on previous work[14] and a recent experiment with nitrogen–vacancy centres[36] using single-photon interference and detection to guarantee deterministic delivery of entangled states at a specified time.

Sample parameters. The designs are very similar to those used previously[27], with only minor parameter modifications. The $\lambda/4$ coplanar waveguide resonators and feed lines are created from etched niobium on a sapphire substrate using standard photolithography techniques (Extended Data Fig. 2a) We define the transmon capacitor pads and junctions with electron-beam lithography and shadow-evaporated aluminium with lift-off. We extract the parameters of the readout circuit (grey elements, Fig. 1b) and transfer circuit (yellow elements, Fig. 1b), as well as the coupling strength of the transmon to these circuits, from fits to the transmission spectra of the respective Purcell filter when the transmon is prepared in its ground or excited state using a technique and model discussed previously[27,37,38]. We obtained four working samples from two fabrication runs, with a standard deviation of approximately 8 MHz in the frequency ν_T of the transfer resonators, and used the pair with the best-matching frequencies. We then tuned the transfer resonators into resonance ($\Delta\nu_T \approx 0.2$ MHz) using the dependence of the resonator dispersive shift[39] on the transmon–resonator detuning $\delta = \nu_{ge} - \nu_T$. To tune the transmon frequencies we use a miniature superconducting coil to thread flux through the superconducting quantum-interference device (SQUID) at each node. Furthermore, the anharmonicity α and the coherence times T_{2ge}^R and T_{2ef}^R of the qutrits are determined using Ramsey-type measurements. We obtain $T_{1ef} \approx T_{1ge}/3$ for the energy decay times T_{1ge} and T_{1ef} of both transmons, which is lower than the expected[40] $T_{1ge}/2$. The excess decay rate may be caused by the more complicated environmental mode structure presented to our transmons due to the set of two resonators with their respective Purcell filters coupled to it. All relevant device parameters are listed in Extended Data Table 1.

Microwave drive schemes. We use resonant Gaussian DRAG[41,42] microwave pulses of length 19.8 ns and 16.8 ns for R_{ge}^π and R_{ef}^π to swap populations between the $|g\rangle$ and $|e\rangle$ states and the $|e\rangle$ and $|f\rangle$ states, respectively. We extract an averaged Clifford-gate fidelity for the $|g\rangle$ and $|e\rangle$ pulses of more than 99.2% for both transmon qubits, from randomized benchmarking experiments[43].

We induce the effective coupling $\tilde{g}$ between states $|f, 0\rangle$ and $|g, 1\rangle$ by applying a microwave tone with drive amplitude ε to the transmon, at the resonance frequency of the transition ($\nu_{f0g1}^A = 4.022$ GHz and $\nu_{f0g1}^B = 3.485$ GHz). Following a procedure described previously[9,30], we calibrate the a.c. Stark shift of the transmon levels induced by the $|f, 0\rangle \leftrightarrow |g, 1\rangle$ drive, and extract the linear relation between the drive amplitude ε and the effective coupling $\tilde{g}$ (Extended Data Fig. 3). To remain in resonance with the driven transition, we adjust the phase of ε on the basis of the measured a.c. Stark shift. We calibrate the drive to reach maximum effective couplings of $\tilde{g}_m^A/(2\pi) = 6.0$ MHz and $\tilde{g}_m^B/(2\pi) = 6.7$ MHz (Extended Data Fig. 3b).

We generate photons with temporal shape $\phi(t) = \frac{1}{2}\sqrt{\kappa_{eff}}\,\text{sech}(\kappa_{eff}t/2)$ by resonantly driving the $|f, 0\rangle \leftrightarrow |g, 1\rangle$ transition with

$$\tilde{g}(t) = \frac{\kappa_{eff}}{4\cosh(\kappa_{eff}t/2)} \frac{1 - e^{\kappa_{eff}t} + (1 + e^{\kappa_{eff}t})\kappa_T/\kappa_{eff}}{\sqrt{(1 + e^{\kappa_{eff}t})\kappa_T/\kappa_{eff} - e^{\kappa_{eff}t}}} \quad (1)$$

where κ_T is the bandwidth of the transfer resonator and $\kappa_{eff} \leq \kappa_T$ is determined by the strength and duration of the transfer pulse. The dynamics are well described by a two-level model with loss, captured by the non-Hermitian Hamiltonian

$$H = \begin{bmatrix} 0 & \tilde{g} \\ \tilde{g}^* & -i\kappa_T/2 \end{bmatrix} \quad (2)$$

where $\tilde{g}^*$ is the complex conjugate of $\tilde{g}$. This Hamiltonian acts on states $|f, 0\rangle$ and $|g, 1\rangle$, analysed in a rotating frame. The non-Hermitian term $-i\kappa_T/2$ accounts for photon emission, which brings the system to the dark state $|g, 0\rangle$. It can be shown that using the effective coupling of equation (1) in the Hamiltonian in equation (2) leads to the emission of a single photon with the desired temporal shape. This analytical solution provides the option of adjusting the effective bandwidth κ_{eff} of the emitted photon and of generating photon shapes with exponential falling and rising edges at rate κ_{eff}. In all experiments, we create photons with the maximum bandwidth achievable in our set-up, limited by κ_T at node A ($\kappa_T^A < \kappa_T^B, 2\tilde{g}_m^A, 2\tilde{g}_m^B$). $\kappa_T^A = \kappa_{eff}$ results in a symmetric amplitude and phase profile of the $|f, 0\rangle \leftrightarrow |g, 1\rangle$ transfer pulse at node A and $\kappa_T^B > \kappa_{eff}$ in an asymmetric drive shape at node B (equation (1)). For the absorption process of the photon we time-reverse the $|f, 0\rangle \leftrightarrow |g, 1\rangle$ drive at node B (Fig. 2g). The photon shape with the shortest pulse duration would require an exponential rising edge proportional to the bandwidth of the receiving node (κ_T^B) and a falling edge proportional to the bandwidth of the emitting node (κ_T^A). In our experiment, we create photons with a symmetric shape, approximately realizing the shortest photon duration.

An alternative protocol to generate a remote-entangled state involves preparing the transmon at node A in $|f, 0\rangle$, swapping half of the population to $|g, 1\rangle$ ($R_{f0g1}^{\pi/2}$) and using the same $|g, 1\rangle \leftrightarrow |f, 0\rangle$ absorption pulse at node B as actually realized in our experiment (Fig. 4a). $R_{f0g1}^{\pi/2}$ can be used to decrease the emission time. However, the absorption process requires the same time. Therefore, in our realization, there is no advantage to using this modified protocol.

Three-level single-shot readout. The state of transmon A (B) is read out with a gated microwave tone applied to the input port of the readout resonator Purcell filter at frequency $\nu_d^A = 4.778$ GHz ($\nu_d^B = 4.765$ GHz). As depicted in Fig. 1b, the output signal is routed through a set of two circulators and a combiner and then amplified at 10 mK with 22 dB (19.3 dB) gain using a Josephson parametric amplifier (JPA). The JPA pump tone is detuned by 2 MHz from the measurement signal and has a bandwidth of 18.3 MHz (32 MHz). Using these JPAs we find a phase-preserving detection efficiency of $\eta = 0.61$ ($\eta = 0.60$) for the full detection line. The signal is then further amplified by a high-electron-mobility transistor (HEMT) at 4 K and two low-noise amplifiers at room temperature. Subsequently, the signal is down-converted to 250 MHz using an analogue mixer, lowpass-filtered, digitized by an analogue-to-digital converter and processed by a field-programmable gate array (FPGA). Within the FPGA, the data are digitally down-converted to d.c. and the corresponding I and Q quadrature values are recorded during a window of 256 ns in 8-ns time steps. The FPGA trigger is timed so that the integration window starts with the rising edge of the measurement pulse. We refer to a recording of the I and Q quadrature of a measurement pulse as a readout trace, $S(t)$.

We prepare the transmon in states $|g\rangle$, $|e\rangle$ and $|f\rangle$ 25,000 times each and record the single-shot traces. Each trace is then integrated in post-processing, with two weight functions, $w_1(t)$ and $w_2(t)$, to obtain the integrated quadratures

$$u = \int S(t)w_1(t)\mathrm{d}t \quad \text{and} \quad v = \int S(t)w_2(t)\mathrm{d}t$$

The collected and integrated traces form three Gaussian-shaped clusters in the u–v plane (Extended Data Fig. 4), which correspond to the Gaussian probability distributions of the trace when the qutrit is prepared in one of the three eigenstates. We model the probability distribution $\boldsymbol{x} = (u, v)$ as a sum of three Gaussian distributions, with density

$$f(\boldsymbol{x}) = \sum_s \frac{A_s}{2\pi\sqrt{|\Sigma|}} \exp\left[-\frac{1}{2}(\boldsymbol{x} - \boldsymbol{\mu}_s)^T \Sigma^{-1}(\boldsymbol{x} - \boldsymbol{\mu}_s)\right]$$

and estimate the parameters A_s, $\boldsymbol{\mu}_s$ and Σ. On the basis of these parameters, we divide the u–v plane into the three regions used to assign the result of the readout of the qutrit state (Extended Data Fig. 4). If an integrated trace is in the region labelled s', then we assign it state s'. By counting the number of traces prepared in state $|s\rangle$ and assigned the value s', we estimate the assignment probabilities $R_{ss'} = P(s'||s\rangle)$ (Extended Data Fig. 4). We optimize the measurement power and signal integration time to minimize the measurement error probability $||I - R||_1/6$, that is, the sum of the off-diagonal elements of the assignment probability matrix (Extended Data Table 2) divided by the number of preparation states. The minimal measurement error probability is realized with an integration time of $t_m^A = 112$ ns ($t_m^B = 216$ ns) and a measurement power that results in a state-dependent photon number in the readout resonator between 0.1 and 2. The probabilities of correct assignment range from 93% to 98% for both qutrits (diagonal elements of Extended Data Table 2).

The probability $M_{s'}$ to assign value s' to a single-shot measurement of a qutrit in state ρ is

$$M_{s'} = P(s' \mid \rho) = \sum_s P(s' \mid s) \rho_{ss}$$

which can be expressed as $\mathbf{M} = R\boldsymbol{\rho}_{\text{diag}}$ where $\boldsymbol{\rho}_{\text{diag}}$ is a vector consisting of the diagonal elements of ρ. The assignment probabilities $\mathbf{M}$ are typically estimated from assignment counts and a first approach to estimate $\boldsymbol{\rho}_{\text{diag}}$ is to equate it to $\mathbf{M}$. This approach is sensitive to measurement errors, but insensitive to state preparation errors. Setting $\boldsymbol{\rho}_{\text{diag}} = R^{-1}\mathbf{M}$ effectively accounts for the effect of single-shot readout error. However, this approach relies on the ability to estimate R precisely and is therefore sensitive to state-preparation error. With transmon reset infidelities of approximately 0.2%[30] and single-qubit gate errors of 0.8% (measured with randomized benchmarking), state-preparation errors are expected to be lower than readout errors. For this reason, we chose to use the latter approach.

We note that the assignment probability matrix $R_{s_A s_B, s'_A s'_B} = P(s'_A s'_B \mid s_A s_B)) = P(s'_A \mid s_A) P(s'_B \mid s_B)$ can be obtained as the outer product of the single-qutrit assignment probability matrices (compiled in Extended Data Table 3) and that we can extend this formalism to correct for single-shot readout errors and extract the state populations of a two-qutrit system.

Estimate of photon loss. We determine the photon loss l_{AB} between node A and node B by emitting a photon in the coherent state $(|0\rangle + |1\rangle)/\sqrt{2}$ first from node A and then from node B independently, as discussed in the main text. Making use of the circulator between the two nodes, we detect the field of each of the emitted photons in the same detection line (Fig. 1). The path travelled by the two emitted photons towards the detector differs only by the length of the waveguide separating the two samples from each other. We evaluate the ratio of the integrated power of the detected fields

$$\frac{\int |\langle a_{\text{out}}^A(t)\rangle|^2 \, dt}{\int |\langle a_{\text{out}}^B(t)\rangle|^2 \, dt}$$

to extract the photon loss l_{AB} between node A and node B. In addition, we estimate the photon loss between node A and B from the specifications of the individual elements connecting the nodes: two printed circuit boards, including connectors (each 2.5% $\pm$ 1%), two coaxial cables of length 0.4 m (each 4.0% $\pm$ 0.1%)[44] and a microwave circulator (13% $\pm$ 2% according to manufacturer). With these parameters we estimate an accumulated photon loss between node A and node B of 24% $\pm$ 3%, in good agreement with the measured value of $l_{AB} = 23.0\% \pm 0.5\%$.

Master-equation simulation. We model the transmons as anharmonic oscillators with annihilation (creation) operators $\hat{b}_i$ ($\hat{b}_i^\dagger$)[10], where the subscript $i \in \{A, B\}$ denotes the emitter and receiver samples, respectively. The transfer resonator annihilation (creation) operators are denoted as $\hat{a}_i$ ($\hat{a}_i^\dagger$). Setting $\hbar = 1$, the driven Jaynes–Cummings Hamiltonian for sample i is

$$\hat{H}^i = \omega_T^i \hat{a}_i^\dagger \hat{a}_i + \omega_{ge}^i \hat{b}_i^\dagger \hat{b}_i + \Omega^i(t)(\hat{b}_i + \hat{b}_i^\dagger) \qquad (3)$$
$$+ g_T^i(\hat{a}_i^\dagger \hat{b}_i + \hat{a}_i \hat{b}_i^\dagger) - \frac{E_C^i}{2}\hat{b}_i^\dagger \hat{b}_i^\dagger \hat{b}_i \hat{b}_i$$

where g_T^i denotes the coupling between the transmon and the transfer resonator, E_C^i denotes the charging energy of the transmon and $\Omega^i(t) = \Omega^i \cos[\omega_d^i t + \varphi^i(t)]$ is the amplitude of the microwave drive that induces the desired coupling $\tilde{g}(t)$. Because the readout resonators do not play a part in the photon transfer dynamics, they are omitted from the Hamiltonian; the static Lamb shifts that they induce are implicitly included in the parameters.

To make the effective coupling $\tilde{g}(t)$ between the $|f, 0\rangle$ and $|g, 1\rangle$ states apparent and to simplify the simulations, we perform a series of unitary transformations on equation (3). We first move to a frame rotating at the drive frequency ω_d^i, and then perform a displacement transformation $\hat{b}_i \rightarrow \hat{b}_i - \beta^i, \hat{a}_i \rightarrow \hat{a}_i - \gamma^i$, choosing β^i and γ^i so that the amplitude of the linear drive terms is set to zero. Next, we perform a Bogoliubov transformation $\hat{b}_i \rightarrow \cos(\Lambda^i)\hat{b}_i - \sin(\Lambda^i)\hat{a}_i, \hat{a}_i \rightarrow \cos(\Lambda^i)\hat{a}_i + \sin(\Lambda^i)\hat{b}_i$ where $\tan(2\Lambda^i) = -2g_T^i / (\omega_T^i - \omega_{ge}^i + 2E_C^i |\beta^i|)$. Neglecting small off-resonant terms, we obtain the resulting effective Hamiltonian

$$\hat{H}_{\tilde{g}}^i = \Delta_T^i \hat{a}_i^\dagger \hat{a}_i + \Delta_{ge}^i \hat{b}_i^\dagger \hat{b}_i + \frac{\alpha^i}{2}\hat{b}_i^\dagger \hat{b}_i^\dagger \hat{b}_i \hat{b}_i + \frac{K^i}{2}\hat{a}_i^\dagger \hat{a}_i^\dagger \hat{a}_i \hat{a}_i$$
$$+ 2\chi_T^i \hat{a}_i^\dagger \hat{a}_i \hat{b}_i^\dagger \hat{b}_i + \frac{1}{\sqrt{2}}(\tilde{g}\hat{b}_i^\dagger \hat{b}_i^\dagger \hat{a}_i + \tilde{g}^* \hat{a}_i^\dagger \hat{b}_i \hat{b}_i) \qquad (4)$$

where $\alpha^i = -E_C^i \cos^4 \Lambda$ is the transmon anharmonicity, $K^i = -E_C^i \sin^4 \Lambda^i$ is the qubit-induced resonator anharmonicity, $\chi_T^i = -E_C^i \cos^2 \Lambda^i \sin^2 \Lambda^i$ is the dispersive shift, $\Delta_T^i = \omega_T^i \cos^2 \Lambda^i + (\omega_{ge}^i - 2E_C^i |\beta^i|^2)\sin^2 \Lambda^i - g_T^i \sin 2\Lambda^i - \omega_d^i$ is the resona-

tor–drive detuning and $\Delta_{ge}^i = (\omega_{ge}^i - 2E_C^i |\beta^i|^2)\cos^2 \Lambda^i + \omega_T^i \sin^2 \Lambda^i + g_T^i \sin 2\Lambda^i - \omega_d^i$ is the qubit–drive detuning. In equation (4), the desired effective coupling $\tilde{g}^i = -E_C^i \beta^i \sqrt{2} \cos^2 \Lambda^i \sin \Lambda^i$ between the $|f, 0\rangle$ and $|g, 1\rangle$ states is now made explicit.

Finally, moving to a frame rotating at Δ_T^i for the resonator and $\Delta_{ge}^i + \alpha^i/2$ for the transmon qubits, the combined effective Hamiltonian of the two samples is

$$\hat{H}_{\text{eff}} = \sum_{i=A,B} \left\{ -\frac{\alpha^i}{2}\hat{b}_i^\dagger \hat{b}_i + \frac{\alpha^i}{2}\hat{b}_i^\dagger \hat{b}_i^\dagger \hat{b}_i \hat{b}_i \right.$$
$$+ \frac{K^i}{2}\hat{a}_i^\dagger \hat{a}_i^\dagger \hat{a}_i \hat{a}_i + 2\chi_T^i \hat{a}_i^\dagger \hat{a}_i \hat{b}_i^\dagger \hat{b}_i$$
$$\left. + \frac{1}{\sqrt{2}}[\tilde{g}^i(t)\hat{b}_i^\dagger \hat{b}_i^\dagger \hat{a}_i + \tilde{g}^i(t)^* \hat{a}_i^\dagger \hat{b}_i \hat{b}_i] \right\}$$
$$- i\frac{\sqrt{\kappa_T^A \kappa_T^B \eta_c}}{2}(\hat{a}_A \hat{a}_B^\dagger - \hat{a}_A^\dagger \hat{a}_B)$$

where η_c is the photon-loss probability of the circulator between the two samples.

Using this effective Hamiltonian, numerical results are obtained by integrating the master equation

$$\dot{\rho} = -i[\hat{H}_{\text{eff}}, \rho]$$
$$+ \kappa_T^A(1-\eta_c)\mathcal{D}[\hat{a}_A]\rho + \mathcal{D}[\sqrt{\kappa_T^A \eta_c}\,\hat{a}_A + \sqrt{\kappa_T^B}\,\hat{a}_B]\rho$$
$$+ \sum_{i=A,B} \{\kappa_{\text{int}}^i \mathcal{D}[\hat{a}_i]\rho + \gamma_{1ge}^i \mathcal{D}[|g\rangle \langle e|_i]\rho$$
$$+ \gamma_{1ef}^i \mathcal{D}[|e\rangle \langle f|_i]\rho \qquad (5)$$
$$+ \sum_{i=A,B} \{\gamma_{\phi ge}^i \mathcal{D}[|e\rangle \langle e|_i - |g\rangle \langle g|_i]\rho$$
$$+ \gamma_{\phi ef}^i \mathcal{D}[|f\rangle \langle f|_i - |e\rangle \langle e|_i]\rho\}$$

where $\mathcal{D}[\hat{O}]\bullet = \hat{O}\bullet\hat{O}^\dagger - \{\hat{O}^\dagger \hat{O}, \bullet\}/2$ denotes the dissipation super-operator, κ_{int}^i the internal decay rates of the resonators, $\gamma_{1nm}^i = 1/T_{1nm}^i$ the decay rates of the transmon qubits between the $|n\rangle_i$ and $|m\rangle_i$ states and $\gamma_{\phi nm}^i = 1/(2T_{1nm}^i) - 1/(T_{2nm}^i)$ the dephasing rates between the $|n\rangle_i$ and $|m\rangle_i$ states of the transmon qubits. The last term in $\hat{H}_{\text{eff}}$ combined with the resonator dissipators in the second line of the master equation (equation (5)), assure that the output of the emitter A is cascaded to the input of the receiver B[45,46] through a circulator with photon loss η_c.

Quantum state and process tomography. Quantum state tomography of a single qutrit is performed by measuring the qutrit state population with the single-shot readout method, after applying the following tomography gates: ${}^xR_{ge}^0$, ${}^xR_{ge}^{\pi/2}$, ${}^yR_{ge}^{\pi/2}$, ${}^xR_{ge}^\pi$, ${}^xR_{ef}^{\pi/2}$, ${}^yR_{ef}^{\pi/2}$, (${}^xR_{ge}^\pi$ ${}^xR_{ef}^{\pi/2}$), (${}^xR_{ge}^\pi$ ${}^yR_{ef}^{\pi/2}$) and (${}^xR_{ge}^\pi$ ${}^xR_{ef}^\pi$). The elements of the density matrix are then reconstructed using a maximum-likelihood method, assuming ideal tomography gates.

To extend this quantum state tomography procedure to two-qutrit density matrices, we perform two local tomography gates (from the 81 pairs of gates that can be formed from the single-qutrit quantum state tomography gates) on transmons A and B, before extracting the state populations using the two-qutrit single-shot measurement method.

To characterize the qubit state transfer from node A to node B, we perform full quantum process tomography[47] (Fig. 3, Extended Data Table 4). We prepare each of the six mutually unbiased qubit basis states[32] $|g\rangle$, $|e\rangle$, $(|g\rangle + |e\rangle)/\sqrt{2}$, $(|g\rangle + i |e\rangle)/\sqrt{2}$, $(|g\rangle - |e\rangle)/\sqrt{2}$ and $(|g\rangle - i |e\rangle)/\sqrt{2}$, transfer the state to node B, then independently measure the qutrit density matrix at node A and node B with quantum state tomography. We obtain the process matrix from these density matrices through linear inversion. Quantum state tomography of the qutrit subspace is required to characterize the residual population in $|f\rangle$ after the qubit state transfer, which is caused mainly by decay from the $|f\rangle$ level in combination with R_{ef}^π swapping $|e\rangle$ with $|f\rangle$ populations. The density matrices that we obtain have a non-unit trace in the qubit subspace, and so does the qubit state transfer process matrix. Consequences of that observation are discussed below for the example of the Bell-state density matrix.

Two-qutrit entanglement. Owing to a residual population of 3.5% of the $|f\rangle$ level of the transmons after the entanglement protocol, the entangled state cannot be described rigorously by a two-qubit density matrix. To be concise, we represent the reconstructed two-qutrit entangled state $\rho_{3\otimes3}$ (Extended Data Fig. 5, Extended Data Table 5) by a two-qubit density matrix ρ_m that consists of the two-qubit elements of $\rho_{3\otimes3}$. This choice of reduction from a two-qutrit to a two-qubit density matrix conserves the state fidelity $\mathcal{F}^s_{|\psi^+\rangle} = \langle\psi^+ |\rho_m| \psi^+\rangle = \langle\psi^+ |\rho_{3\otimes3}| \psi^+\rangle$; however, ρ_m has a non-unit trace. In addition, this reduction method gives a

conservative estimate of the concurrence $\mathcal{C}(\rho_{\mathrm{m}})$ compared to a projection of $\rho_{3\otimes3}$ on the set of physical two-qubit density matrices.

To verify the three-level bipartite entanglement, we use the computable cross-norm or realignment criterion[48], which is well defined for multi-level mixed entangled states. This criterion states that a state ρ must be entangled if $\sum_k \lambda_k > 1$, with $\rho = \sum_k \lambda_k G_k^A \otimes G_k^B$ and $G_k^{A(B)}$ an orthonormal basis of the observable spaces of $\mathcal{H}^{A(B)}$. We obtain $\sum_k \lambda_k = 1.612 \pm 0.003$ with the measured entangled state $\rho_{3\otimes3}$, providing unambiguous evidence for the existence of entanglement of the prepared state.

Data availability. The data that support the findings of this study are available within the paper.

34. Verstraete, F. & Wolf, M. M. Entanglement versus bell violations and their behavior under local filtering operations. *Phys. Rev. Lett.* **89**, 170401 (2002).
35. Dickel, C. et al. Chip-to-chip entanglement of transmon qubits using engineered measurement fields. *Phys. Rev. B* **97**, 064508 (2018).
36. Humphreys, P. C. et al. Deterministic delivery of remote entanglement on a quantum network. Preprint at https://arxiv.org/abs/1712.07567 (2017).
37. Jeffrey, E. et al. Fast accurate state measurement with superconducting qubits. *Phys. Rev. Lett.* **112**, 190504 (2014).
38. Sete, E. A., Martinis, J. M. & Korotkov, A. N. Quantum theory of a bandpass Purcell filter for qubit readout. *Phys. Rev. A* **92**, 012325 (2015).
39. Wallraff, A. et al. Approaching unit visibility for control of a superconducting qubit with dispersive readout. *Phys. Rev. Lett.* **95**, 060501–060504 (2005).
40. Peterer, M. J. et al. Coherence and decay of higher energy levels of a superconducting transmon qubit. *Phys. Rev. Lett.* **114**, 010501 (2015).
41. Motzoi, F., Gambetta, J. M., Rebentrost, P. & Wilhelm, F. K. Simple pulses for elimination of leakage in weakly nonlinear qubits. *Phys. Rev. Lett.* **103**, 110501 (2009).
42. Gambetta, J. M., Motzoi, F., Merkel, S. T. & Wilhelm, F. K. Analytic control methods for high-fidelity unitary operations in a weakly nonlinear oscillator. *Phys. Rev. A* **83**, 012308–012313 (2011).
43. Chow, J. M. et al. Randomized benchmarking and process tomography for gate errors in a solid-state qubit. *Phys. Rev. Lett.* **102**, 090502 (2009).
44. Kurpiers, P., Walter, T., Magnard, P., Salathe, Y. & Wallraff, A. Characterizing the attenuation of coaxial and rectangular microwave-frequency waveguides at cryogenic temperatures. *EPJ Quant. Technol.* **4**, 8 (2017).
45. Gardiner, C. W. Driving a quantum system with the output field from another driven quantum system. *Phys. Rev. Lett.* **70**, 2269–2272 (1993).
46. Carmichael, H. J. Quantum trajectory theory for cascaded open systems. *Phys. Rev. Lett.* **70**, 2273–2276 (1993).
47. Chuang, I. L. & Nielsen, M. A. Prescription for experimental determination of the dynamics of a quantum black box. *J. Mod. Opt.* **44**, 2455–2467 (1997).
48. Gühne, O. & Tóth, G. Entanglement detection. *Phys. Rep.* **474**, 1–75 (2009).
49. Bell, J. S. On the Einstein Podolsky Rosen paradox. *Phys. Phys. Fiz.* **1**, 195–200 (1964).
50. Clauser, J. F., Horne, M. A., Shimony, A. & Holt, R. A. Proposed experiment to test local hidden-variable theories. *Phys. Rev. Lett.* **23**, 880–884 (1969).
51. Chou, C.-W. et al. Functional quantum nodes for entanglement distribution over scalable quantum networks. *Science* **316**, 1316–1320 (2007).
52. Laurat, J., Choi, K. S., Deng, H., Chou, C. W. & Kimble, H. J. Heralded entanglement between atomic ensembles: preparation, decoherence, and scaling. *Phys. Rev. Lett.* **99**, 180504 (2007).
53. Yuan, Z.-S. et al. Experimental demonstration of a BDCZ quantum repeater node. *Nature* **454**, 1098–1101 (2008).
54. Matsukevich, D. N., Maunz, P., Moehring, D. L., Olmschenk, S. & Monroe, C. Bell inequality violation with two remote atomic qubits. *Phys. Rev. Lett.* **100**, 150404 (2008).
55. Maunz, P. et al. Heralded quantum gate between remote quantum memories. *Phys. Rev. Lett.* **102**, 250502 (2009).
56. Hucul, D. et al. Modular entanglement of atomic qubits using photons and phonons. *Nat. Phys.* **11**, 37–42 (2015).
57. Lettner, M. et al. Remote entanglement between a single atom and a Bose-Einstein condensate. *Phys. Rev. Lett.* **106**, 210503 (2011).
58. Usmani, I. et al. Heralded quantum entanglement between two crystals. *Nat. Photon.* **6**, 234–237 (2012).
59. Pfaff, W. et al. Unconditional quantum teleportation between distant solid-state quantum bits. *Science* **345**, 532–535 (2014).
60. Hensen, B. et al. Loophole-free bell inequality violation using electron spins separated by 1.3 kilometres. *Nature* **526**, 682–686 (2015).
61. Narla, A. et al. Robust concurrent remote entanglement between two superconducting qubits. *Phys. Rev. X* **6**, 031036 (2016).
62. Stockill, R. et al. Phase-tuned entangled state generation between distant spin qubits. *Phys. Rev. Lett.* **119**, 010503 (2017).
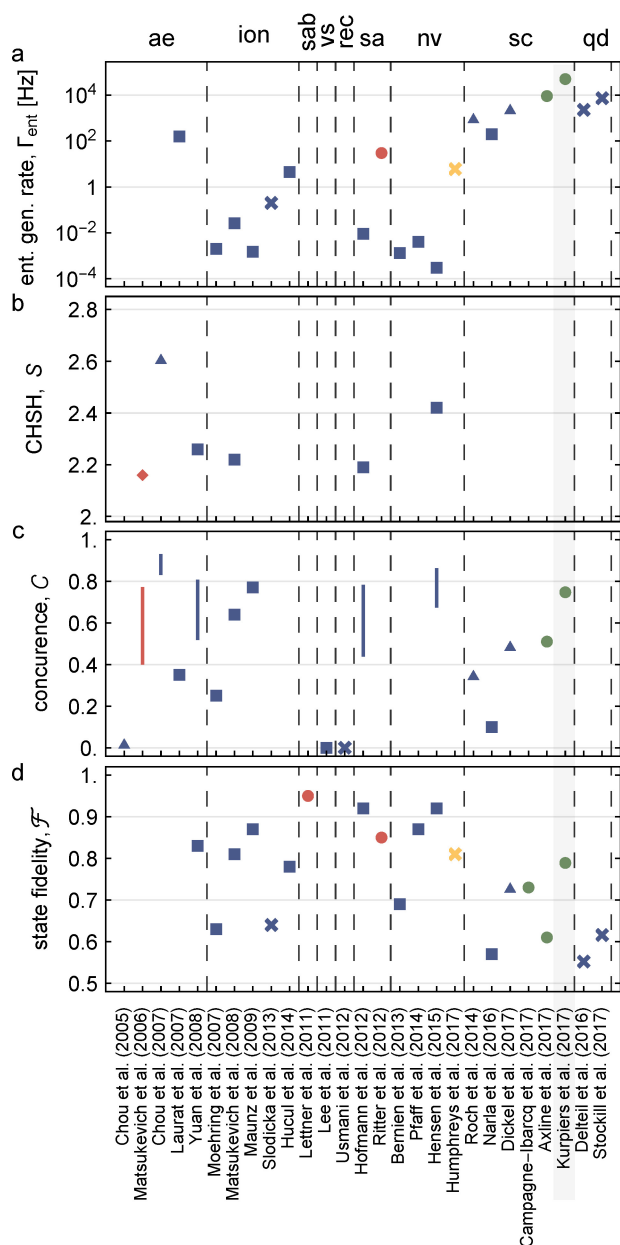
**Extended Data Fig. 1 | Overview of remote-entanglement experiments.**
a, Entanglement generation rate Γ_{ent}. **b**, CHSH–Bell inequality[49,50]
correlation S. **c**, Concurrence $\mathcal{C}$. **d**, Entangled state fidelity $\mathcal{F}^s$. The
experiments are grouped by physical system: atomic ensembles
('ae')[12,21,51–53], trapped ions ('ion')[15,17,54–56], single-atom Bose–Einstein
condensate ('sab')[57], vibrational state of diamonds ('vs')[18], rare-Earth-
doped crystals ('rec')[58], single atoms ('sa')[19,22], nitrogen–vacancy centres
('nv')[20,36,59,60], superconducting circuits ('sc')[14,23,24,35,61] or quantum dots
('qd')[16,62]. The colours indicate different implementations: probabilistic
unheralded (red), probabilistic heralded (blue), guaranteeing a
deterministic delivery of an entangled state at a pre-specified time (yellow)
or fully deterministic (green). The plot markers indicate different schemes
for realizing the remote interaction: measurement-induced (triangles),
single-photon (crosses) or two-photon (squares) interference and
detection, direct transfer (diamond) or direct transfer with shaped photons
(circles). The lines in **c** are bounds[34] on the concurrence $\mathcal{C}$ calculated from
measured CHSH–Bell correlations S. The shaded column highlights this
study.
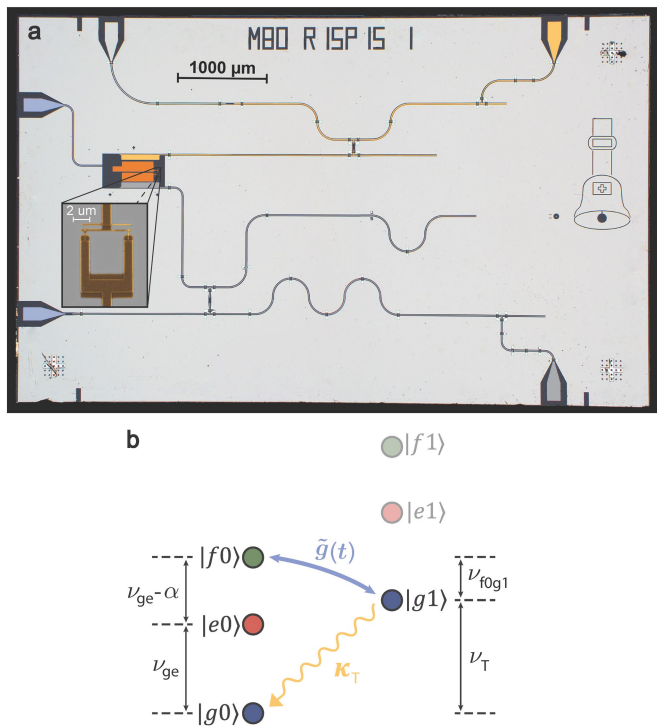
Extended Data Fig. 2 | Micrograph of sample and energy-level diagram.
a, False-colour micrograph of a sample of the same design co-fabricated
with the one used for node A. The circuit elements are colour coded as in
Fig. 1: transfer circuit (yellow), readout circuit (grey), transmon (orange)
and input lines of the transmon and readout circuit (blue). The input
to the transfer circuit is used as an auxiliary port to perform resonator
spectroscopy in transmission. The inset shows a scanning electron
microscopy (SEM) micrograph of the asymmetric SQUID with a ratio of
5:1 between the areas of the Josephson junctions used in the transmon.
b, Schematic of the energy-level diagram of the coupled transmon-transfer
resonator system. The numerical values of all parameters are listed in
Extended Data Table 1.
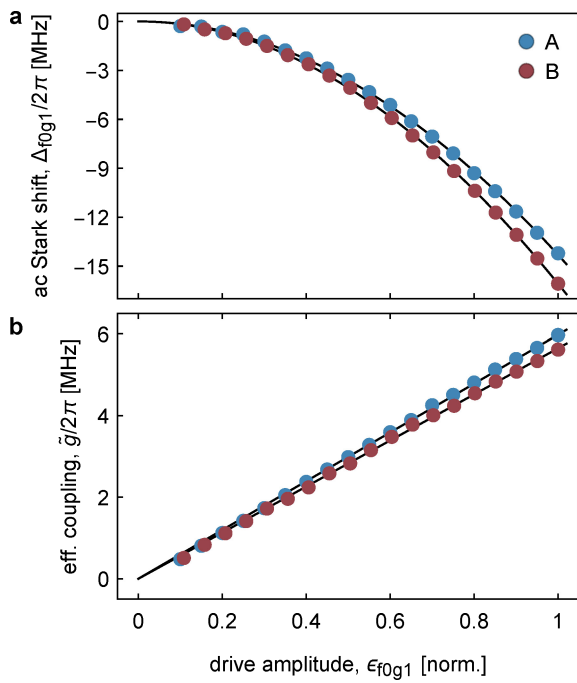
Extended Data Fig. 3 | a.c. Stark shift and Rabi rate of the $|f, 0\rangle \leftrightarrow |g, 1\rangle$
transition. a, b, Measurement (filled circles) of the a.c. Stark shift $\Delta_{f0g1}/$
(2π) (**a**) and the effective coupling $\widetilde{g}/(2\pi)$ of the $|f, 0\rangle \leftrightarrow |g, 1\rangle$ transition
(**b**) versus drive amplitude ε_{f0g1} for sample A (blue) and B (red). The solid
lines in **a** (**b**) are quadratic (linear) fits to the data[30].
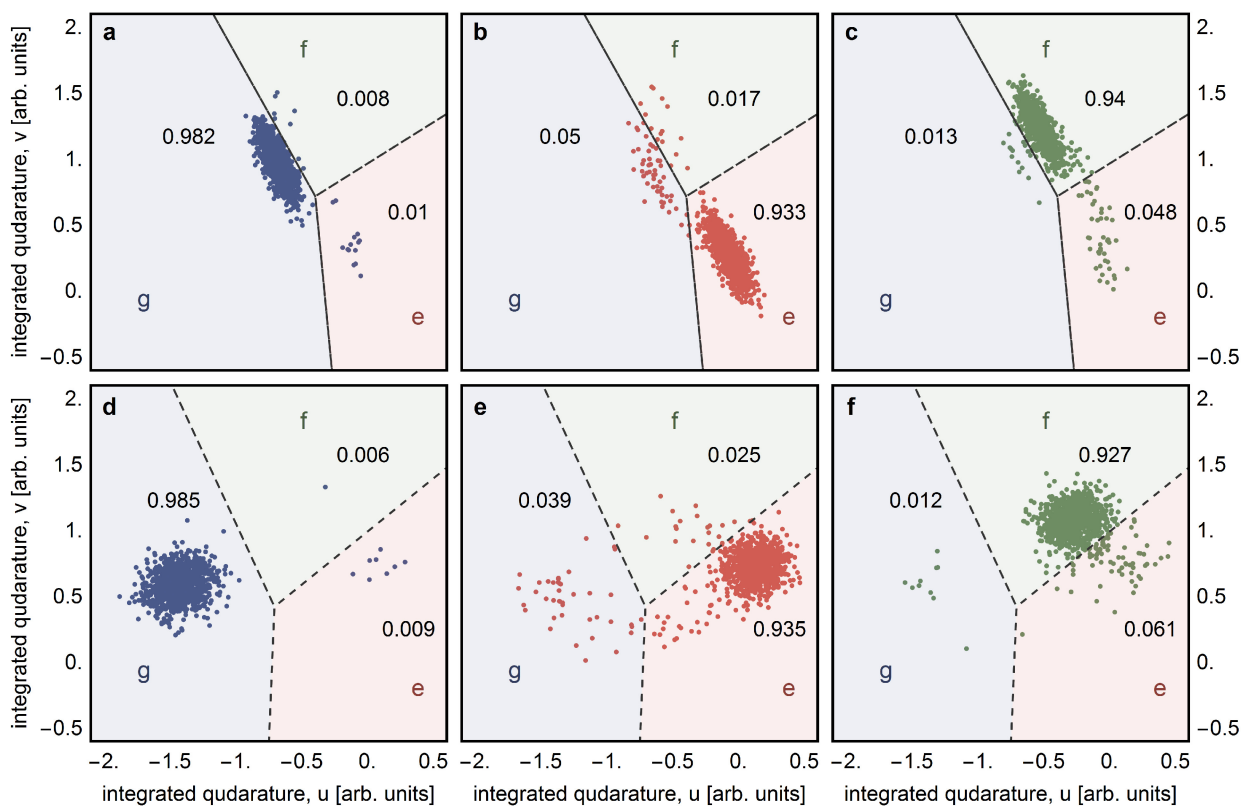
Extended Data Fig. 4 | Qutrit single-shot readout characterization.
a–f, Scatter plot of the measured integrated quadrature values u and v for qutrit A (**a–c**) and B (**d–f**) when prepared in state $|g\rangle$ (blue; **a, d**), $|e\rangle$ (red; **b, e**) and $|f\rangle$ (green; **c, f**). We plot only the first 1,000 of the 25,000 repetitions for each state-preparation experiment. The dashed lines are the qutrit-state discrimination thresholds used to obtain the assignment probabilities (numbers, which are also listed in Extended Data Table 2).
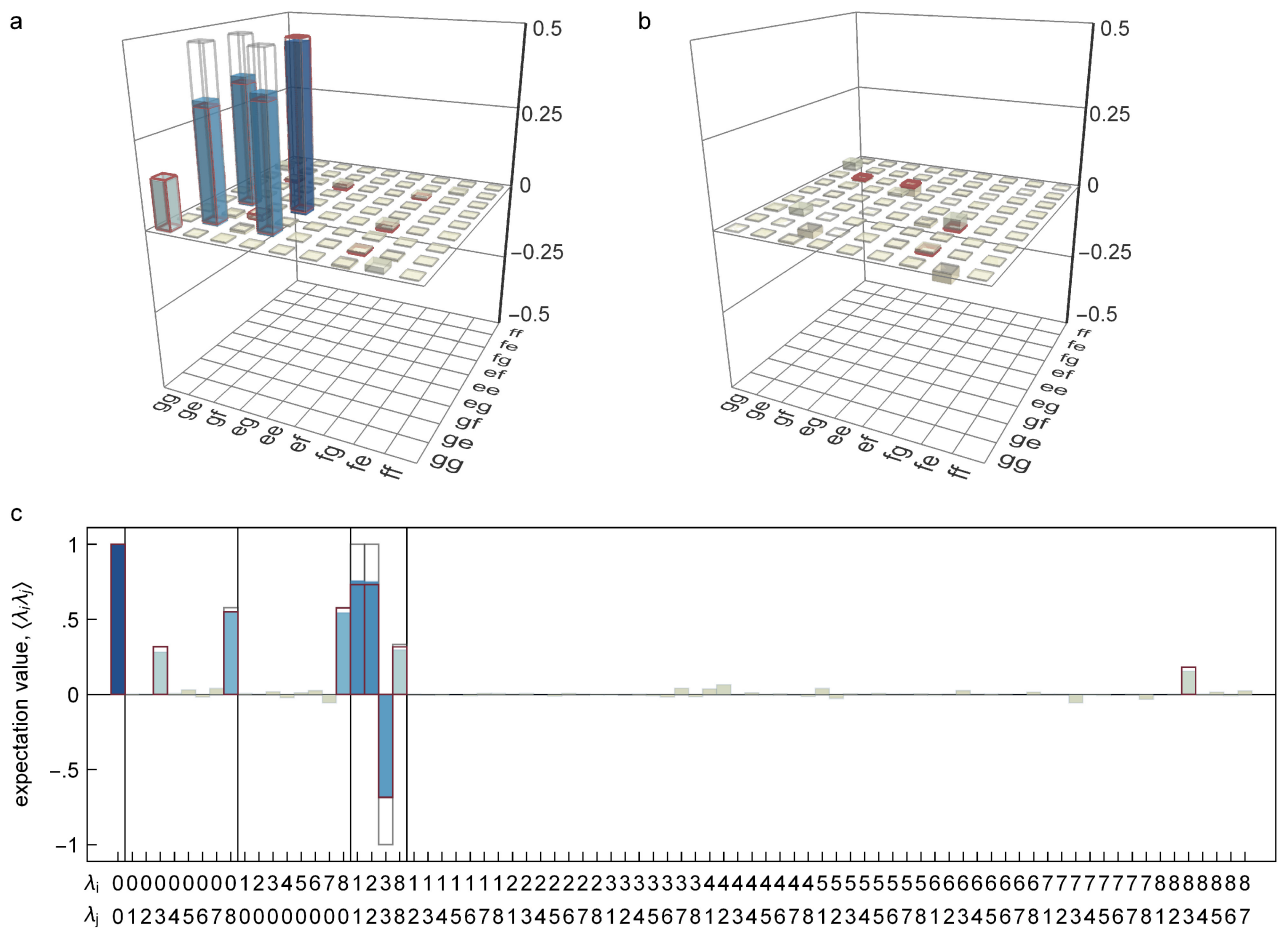
Extended Data Fig. 5 | Characterization of entangled states in a two-qutrit basis. a–c, Two-qutrit state tomography: real (**a**) and imaginary (**b**) part of the density matrix and expectation values of the Gell–Mann operators λ_k (**c**). The ideal Bell state $|\psi^+\rangle$ and numerical master-equation simulation are depicted as grey and red outlines, respectively. λ_0 denotes the identity operation, $\lambda_{1,2,3}$ denote the Pauli matrices $\sigma_{x,y,z}^{ge}$ in the qubit subspace, $\lambda_{4,5}$ correspond to $\sigma_{x,y}^{gf}$, $\lambda_{6,7}$ correspond to $\sigma_{x,y}^{ef}$ and λ_8 is the diagonal matrix $(\sigma_z^{ge} + 2\sigma_z^{ef}) / \sqrt{3}$. The trace distance between the measurement and the simulation is 0.107.

Extended Data Table 1 | Summary of device parameters for nodes A and B

quantity, symbol (unit)	Node A	Node B
readout resonator frequency, ν_{R} (GHz)	4.787	4.780
readout Purcell filter frequency, ν_{Rpf} (GHz)	4.778	4.780
readout resonator bandwidth, $\kappa_R/2\pi$ (MHz)	12.6	27.1
readout circuit dispersive shift, $\chi_R/2\pi$ (MHz)	5.8	11.6
transfer resonator frequency, ν_{T} (GHz)	8.4005	8.4003
transfer Purcell filter frequency, ν_{Tpf} (GHz)	8.426	8.415
transfer resonator bandwidth, $\kappa_T/2\pi$ (MHz)	10.4	13.5
transfer circuit dispersive shift, $\chi_T/2\pi$ (MHz)	6.3	4.7
qubit transition frequency, ν_{ge} (GHz)	6.343	6.096
transmon anharmonicity, α (MHz)	-265	-308
$|f,0\rangle \leftrightarrow |g,1\rangle$ transition frequency, ν_{f0g1} (GHz)	4.022	3.485
$|f,0\rangle \leftrightarrow |g,1\rangle$ max. eff. coupling, $\tilde{g}_{\mathrm{m}}/2\pi$ (MHz)	6.0	6.7
energy relaxation time on ge, T_{1ge} (μs)	4.9	4.6
energy relaxation time on ef, T_{1ef} (μs)	1.6	1.4
coherence time on ge, $T_{\mathrm{2ge}}^{\mathrm{R}}$ (μs)	3.4	2.6
coherence time on ef, $T_{\mathrm{2ef}}^{\mathrm{R}}$ (μs)	2.1	0.9

Extended Data Table 2 | Probabilities of identifying the prepared states (columns) as the measured states (rows) for qutrits A and B

	Qutrit A			Qutrit B			
	$|g\rangle$	$|e\rangle$	$|f\rangle$	$|g\rangle$	$|e\rangle$	$|f\rangle$	
g	98.2	5.0	1.3	98.5	3.9	1.2	g
e	1.0	93.3	4.8	0.9	93.5	6.1	e
f	0.8	1.7	94.0	0.6	2.5	92.7	f

The diagonal elements show correct identification; the off-diagonal elements show misidentifications.

Extended Data Table 3 | Probabilities of identifying the prepared input states (columns) as the indicated output states (rows) for all possible tuples of two-qutrit basis states

	$\lvert gg\rangle$	$\lvert ge\rangle$	$\lvert gf\rangle$	$\lvert eg\rangle$	$\lvert ee\rangle$	$\lvert ef\rangle$	$\lvert fg\rangle$	$\lvert fe\rangle$	$\lvert ff\rangle$
gg	96.8	3.9	1.1	4.9	0.2	0.1	1.2	0.0	0.0
ge	0.9	91.9	6.0	0.0	4.7	0.3	0.0	1.2	0.1
gf	0.6	2.5	91.1	0.0	0.1	4.6	0.0	0.0	1.2
eg	1.0	0.0	0.0	91.9	3.7	1.1	4.7	0.2	0.1
ee	0.0	0.9	0.1	0.8	87.3	5.7	0.0	4.5	0.3
ef	0.0	0.0	0.9	0.6	2.4	86.5	0.0	0.1	4.4
fg	0.8	0.0	0.0	1.6	0.1	0.0	92.5	3.7	1.1
fe	0.0	0.7	0.0	0.0	1.6	0.1	0.8	87.9	5.8
ff	0.0	0.0	0.7	0.0	0.0	1.6	0.6	2.4	87.1

The diagonal elements show correct identification; the off-diagonal elements show misidentifications.

Extended Data Table 4 | Numerical values of the experimentally obtained process-matrix elements of the qubit state transfer

	I	X	$\tilde{Y}$	Z
I	0.8002	0.0008-0.0021i	-0.0036-0.0033i	0.0818-0.0038i
X	0.0008+0.0021i	0.0748	-0.0734	0.0017+0.0037i
$\tilde{Y}$	-0.0036+0.0033i	-0.0734	0.0727	0.0011+0.0028i
Z	0.0818+0.0038i	0.0017-0.0037i	0.0011-0.0028i	0.0313

The absolute value of this process matrix is depicted in Fig. 3 as coloured bars.

Extended Data Table 5 | Numerical values of the experimentally obtained density-matrix elements of the two-qubit remote-entangled state in a two-qutrit basis

	gg	ge	gf	eg	ee	ef	fg	fe	ff
gg	0.142	-0.001	0.002-0.005i	0.001-0.001i	0.001-0.001i	0.001	-0.006-0.004i	0.016-0.027i	0.001+0.001i
ge	-0.001	0.343	-0.008-0.021i	0.378	0.003+0.002i	-0.003-0.004i	0.003+0.006i	-0.005-0.002i	0.001
gf	0.002+0.005i	-0.008+0.021i	0.015	-0.004	-0.002	-0.001-0.002i	0.005-0.002i	0.002-0.001i	0.
eg	0.001+0.001i	0.378	-0.004	0.48	0.002-0.001i	0.001-0.01i	0.013+0.029i	-0.002-0.001i	0.002
ee	0.001+0.001i	0.003-0.002i	-0.002	0.002+0.001i	0.	0.	-0.001	0.	0.
ef	0.001	-0.003+0.004i	-0.001+0.002i	0.001+0.01i	0.	0.001	-0.001+0.002i	0.	0.
fg	-0.006+0.004i	0.003-0.006i	0.005+0.002i	0.013-0.029i	-0.001	-0.001-0.002i	0.012	0.001+0.001i	0.
fe	0.016+0.027i	-0.005+0.002i	0.002+0.001i	-0.002+0.001i	0.	0.	0.001-0.001i	0.007	0.
ff	0.001-0.001i	0.001	0.	0.002	0.	0.	0.	0.	0.

The real and imaginary parts of this density matrix are depicted as coloured bars in Extended Data Fig. 5a and b, respectively.